

# Flux Balancing of Light and Nutrients in a Biofilm Photobioreactor for Maximizing Photosynthetic Productivity

Thomas E. Murphy and Halil Berberoglu

Mechanical Engineering Dept., Cockrell School of Engineering, The University of Texas at Austin, Austin, TX 78712

DOI 10.1002/btpr.1881

Published online in Wiley Online Library (wileyonlinelibrary.com)

*This article reports a combined experimental and numerical study on the efficient operation of Porous Substrate Bioreactors. A comprehensive model integrating light transport, mass transport, and algal growth kinetics was used to understand the productivity of photosynthetic biofilms in response to delivery rates of photons and nutrients. The reactor under consideration was an evaporation driven Porous Substrate Bioreactor (PSBR) cultivating the cyanobacteria *Anabaena variabilis* as a biofilm on a porous substrate which delivers water and nutrients to the cells. In an unoptimized experimental case, this reactor was operated with a photosynthetic efficiency of 2.3%, competitive with conventional photobioreactors. Moreover, through a scaling analysis, the location at which the phosphate delivery rate decreased the growth rate to half of its uninhibited value was predicted as a function of microorganism and bioreactor properties. The numerical model along with the flux balancing techniques presented herein can serve as tools for designing and selecting operating parameters of biofilm based cultivation systems for maximum productivity. © 2014 American Institute of Chemical Engineers *Biotechnol. Prog.*, 000:000–000, 2014*

**Keywords:** biofilm photobioreactors, nutrient limitation, light transport, mass transport, productivity modeling

## Introduction

Algae cultivation has a wide variety of applications, including but not limited to wastewater remediation, production of food supplements, high value chemicals, and biofuels, as well as life support of humans in space.<sup>1–5</sup> Traditionally, algae has been cultivated in open ponds or closed photobioreactors, both of which employ suspended cell culturing.<sup>6,7</sup> Suspended culturing suffers from several drawbacks, including requirements for large working water volume and large energy inputs for pumping and mixing the culture, as well as dewatering and concentrating the biomass during harvesting.<sup>8,9</sup>

In light of these challenges, biofilm photobioreactors have been proposed in which algae are cultivated attached to a solid surface rather than in suspension.<sup>10–12</sup> The large microorganism densities characteristic of such photobioreactors significantly reduce the working water volume and associated energy input requirements.<sup>10</sup> However, a flowing liquid layer is still required adjacent to the biofilm to keep the cells hydrated and provide nutrients, which limits the potential for reducing the water and energy input.

Recently, a subclass of biofilm photobioreactors has been presented wherein algae are cultivated as a biofilm attached to a porous substrate which delivers water and nutrients to the microorganisms.<sup>5,13,14</sup> Such systems, here referenced as porous substrate bioreactors (PSBRs), further reduce the water and energy input requirements for cultivation. Moreover, having an array of vertical units in a given volume

enhances the illuminated surface area to volume ratio of the photobioreactor system, which has been shown to enhance productivity.<sup>15</sup> Moreover, gas transfer is also enhanced in PSBRs compared to other cultivation systems due to (i) the increased surface area to volume ratio and (ii) the microorganisms being in direct contact with the gas phase.

However, PSBRs introduce a new set of engineering challenges. For example, nutrient delivery to the cells is accomplished by diffusion, rather than advection, which motivates the concern that growth in these systems could be diffusion-limited. An optimally designed system is one that delivers nutrients to the cells at the rate at which the cells would consume them based on the local photon availability. This strategy enables maximum photon utilization by avoiding nutrient limited and nutrient inhibited growth. Thus, it is first necessary to understand the transport of light and mass in the bioreactor in relation to the growth kinetics.

This study addresses this need and reports a comprehensive model integrating light transport, mass transport, and growth kinetics in a general PSBR setting. The model is applied to a novel evaporation driven PSBR and provides insight into optimizing this system by balancing the fluxes of dissolved nutrients and photons to the cells.

## Current State of Knowledge

### Porous substrate bioreactor (PSBR) technology

Naumann et al. cultivated a variety of green algae and diatom strains on a Twin-Layer Photobioreactor (TLP) for generation of aquaculture feed.<sup>14</sup> The TLP consisted of multiple

Correspondence concerning this article should be addressed to: H. Berberoglu at berberoglu@mail.utexas

vertical planar units. Each vertical unit consisted of a non-woven glass fiber inner layer and outer paper layers, which hosted microbial growth, on either side of the inner layer. The pore size of the paper was small enough that the microorganisms could not cross into the inner layer, but large enough to enable nutrient diffusion. A pump was used to circulate nutrient medium through the inner layer, and water and nutrients were delivered to the cells by wicking and diffusion. A combination of solar light and sodium discharge lamps was used to provide the cells with a 15 h/9 h light/dark cycle, where the average irradiance during the light period was  $67 \mu\text{E}/\text{m}^2 \text{ s}$ . The authors reported growth rates for *Phaeodactylum tricornutum*, *Tetraselmis suecica*, *Nannochloropsis* sp., and *Isochrysis* sp. of 1.8, 1.5, 0.8, and 0.6 g of biomass per square meter of biofilm area per day, respectively.

Moreover, Liu et al. reported a similar system in which microalgae were cultivated on vertical sheets of filter paper, each supported by a solid glass pane.<sup>13</sup> A drip system was used to deliver nutrient medium into the filter paper from the top. The authors constructed multiple parallel vertical panes and defined the light dilution ratio as the ratio of the substrate surface area to the footprint area of the reactor. Using a light dilution ratio of 10 under outdoor solar lighting, the average biomass productivity over a cultivation period of eight days was 65 g of *Scenedesmus obliquus* per square meter of footprint area per day.

Finally, Murphy et al. constructed and operated a Surface-Adhering Bioreactor (SABR) to cultivate the cyanobacteria *Anabaena variabilis*.<sup>5</sup> The reactor consisted of ten vertical porous ribs that hosted cyanobacterial growth on each side. The bottom of each rib was immersed in a nutrient medium flow channel. The top region of the rib was exposed to ambient air, and evaporation from this region drove the flow of nutrient medium through the rib, mimicking the transpirative operation of a tree. Therefore, in contrast to the aforementioned attached photobioreactors, the SABR did not require an active pump for operation. The top horizontal surface of the reactor was subjected to an irradiance of  $74 \pm 9 \mu\text{E}/\text{m}^2 \text{ s}$  using cool white fluorescent bulbs for a cultivation period of 21 days, during which the cyanobacterial growth rate was approximately 0.5 g per square meter of footprint area per day.

### Biofilm modeling

A vast body of research exists on modeling the formation, growth, metabolic rates, and death of nonphotosynthetic biofilms.<sup>16–18</sup> Such modeling studies have predominantly been motivated by (i) design and optimization of engineered biofilm systems, such as wastewater bioreactors, and (ii) eliminating undesirable biofilms, which can cause infectious diseases, increase drag on the hulls of ships, decrease heat transfer rates through pipes, and corrode metals.<sup>16</sup> Modeling of PSBRs presents two unique challenges compared to previously reported modeling efforts. First, the previously reported biofilm models consider the biofilm at the interface of a bulk liquid layer and an impermeable solid substratum,<sup>16</sup> whereas in PSBRs the biofilm is at the interface of a porous substratum and the gas phase.<sup>5,13,14</sup> Second, most previous studies have focused on nonphotosynthetic biofilms in which light availability to cells is not a parameter.

More recent studies have presented models of photosynthetic biofilms in photobioreactors for hydrogen production.<sup>19,20</sup> Liao et al. modeled photosynthetic biofilm growth

on a solid surface in a flat panel photobioreactor using the lattice Boltzmann method.<sup>19</sup> The authors employed a two-dimensional model that took into account diffusion, consumption, and production, and modeled growth using the cellular automata method.<sup>21</sup> The authors investigated the effects of initial inoculation concentration, light intensity, and pH on biofilm growth rate. However, their model assumed uniform light intensity within the biofilm, which is not a realistic assumption as light attenuates exponentially over the thickness of the biofilm, giving rise to significant intensity gradients.<sup>22</sup>

The current study reports experimental results on the productivity of a novel type of PSBR driven by evaporation and capillary forces. Moreover, this study presents for the first time an integrated light transport, mass transport, and growth kinetic modeling framework for virtually investigating and optimizing PSBRs. The model provides insight into the local fluxes of photons, nutrients, and inhibitory metabolites such as oxygen within the biofilm and their influence on cellular growth kinetics. Thus, the model can be used to design PSBRs that deliver photons and nutrients to cells at optimal rates maximizing productivity and nutrient utilization.

## Materials and Methods

An experimental setup was designed to cultivate and monitor evaporation driven PSBRs. For this, first, biofilms with uniform thickness were cultivated on porous substrates. Then, the biofilm-porous substrate assembly was operated as a PSBR while monitoring the nutrient medium flow rate through the reactor and biomass productivity in real time.

### Microorganism and nutrient medium

The cyanobacterium *Anabaena variabilis* (ATCC 29413) was acquired from NASA Ames Research Center. The BG11 nutrient medium was used.<sup>23</sup>

### Batch microorganism cultivation

Prior to cultivation of the biofilms, the organisms were grown in 2 L bottles, continuously illuminated with fluorescent bulbs with a color temperature of 4100 K at a mean surface photon flux density of  $74 \pm 8 \mu\text{E}/\text{m}^2 \text{ s}$  ( $16 \pm 2 \text{ W}/\text{m}^2$ ) and sparged with air containing  $3 \pm 1\%$  v/v  $\text{CO}_2$  at a rate of 400 mL/min. The culture temperature was  $27 \pm 3^\circ\text{C}$  throughout the batch cultivation period.

### Cultivation of biofilms with uniform thickness

Uniform biofilm thickness was a requirement of the numerical model. Therefore, a custom photobioreactor was designed to cultivate uniform thickness biofilms on porous substrates. The porous substrates were glass fiber filter paper strips (Whatman, 934-AH) measuring 90 mm long by 13 mm wide by 0.4 mm thick, and having a particle retention size of 1.5  $\mu\text{m}$ . The strips were inoculated by spraying a planktonic culture through a rectangular mask, resulting in a growth area measuring 60 mm long (in the direction of flow) and 7 mm wide. The initial biomass density was approximately 0.2 g/m<sup>2</sup>. Each porous strip was then placed on a rectangular Parafilm sheet with a rectangular hole. The porous strip-Parafilm assembly was then placed on top of the surface of a 400 mL sample of BG11 nutrient medium in a

500 mL acrylic box. In this way, the bottom surfaces of the porous strips were in contact with the liquid medium and the microorganisms themselves were in contact with the head space of the box. The box was covered with a transparent sheet to enable light transmission and prevent evaporation from the biofilm surfaces. The biofilms were continuously illuminated with fluorescent bulbs with a color temperature of 4100 K at a mean surface photon flux density of  $74 \pm 8 \mu\text{E}/\text{m}^2 \text{ s}$  ( $16 \pm 2 \text{ W}/\text{m}^2$ ) for 3 days.

### PSBR operation

The evaporation driven PSBR used in this study is shown in Figure 1. This laboratory scale reactor enabled precise control of the gas phase surrounding the biofilm and real time monitoring of biofilm productivity. As such, it differed from a scaled up PSBR in that the latter generally consists of multiple vertical biofilm units rather than a single horizontal one.<sup>5,13,14</sup> In the evaporation driven PSBR used in this study, one end of the porous substrate was in contact with a nutrient medium reservoir and the other end was in contact with a terminal porous end. Evaporation from the terminal end drove nutrient medium flow through the reactor. The biofilm growth region was enclosed in a transparent chamber for environmental control. Evaporation from the biofilm surface, and therefore salt accumulation in the biofilm, was mitigated by keeping water vapor in the interior air at its saturation pressure, whereas the terminal end was exposed to room air. In this way, the terminal end also served as a collection region for unused salts and bioproducts secreted by the microorganisms. The terminal end can be periodically replaced to collect these products and regenerate the vascular structure of the reactor.

### PSBR cultivation parameters

The biofilm was continuously illuminated with fluorescent bulbs (Philips, color temperature 4100 K) at a photon flux density of  $110 \pm 5 \mu\text{E}/\text{m}^2 \text{ s}$  ( $24 \pm 1 \text{ W}/\text{m}^2$ ) PAR. The transparent acrylic test chamber used to house the biofilm measured 8 cm long, 3.2 cm wide, and 1.0 cm tall. Gas was continuously supplied to the chamber at a rate of  $3 \pm 1 \text{ mL}/\text{min}$ . The steady state partial pressures of  $\text{CO}_2$  and  $\text{O}_2$  in the gas phase inside the reactor were measured with a gas chromatograph (Shimadzu, GC-2014a) and were 47 Pa (19  $\mu\text{mol}/\text{L}$ ) and 21 kPa (8.6 mmol/L), respectively. The temperature inside the chamber throughout the duration of the experiment was  $25.0 \pm 0.5^\circ\text{C}$ . The relative humidity was measured with a relative humidity sensor with an accuracy of 3.5% (Honeywell, HIH-4021-001), and was 100% throughout the duration of the

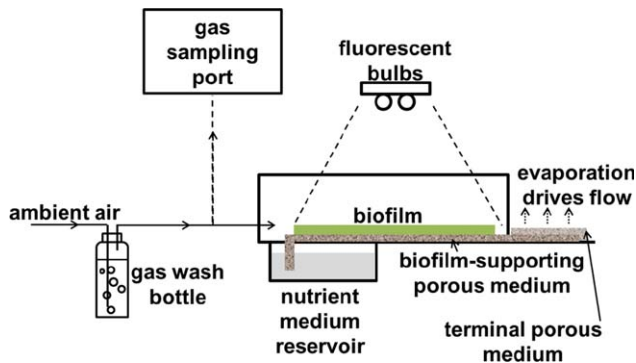


Figure 1. Schematic of the experimental setup.

experiments. The nutrient medium flow rate was quantified by measuring the rate of change of the mass of nutrient medium in the reservoir. The superficial nutrient medium velocity,  $u_p$ , was calculated by dividing the flow rate by the cross sectional area of the porous medium.

### Measurement of biomass concentration

The local areal biomass concentration,  $X_A$ , expressed in grams dry weight per square meter ( $\text{g}/\text{m}^2$ ), was measured using the multispectral imaging technique presented by Murphy et al.<sup>24</sup> Briefly, this method uses an RGB digital image of the biofilm to recover its biomass concentration using correlations between biomass and image color that were generated under the same background and lighting conditions as the experimental setup. The areal biomass concentration was periodically measured at six discretized regions along the length of the biofilm. The biomass production rate in each region was calculated by fitting a least squares regression line to the data of areal biomass concentration versus time over a cultivation period of 24 h. Experiments were performed in duplicate.

### Modeling Analysis

Figure 2 shows the schematic of the PSBR under analysis. In this system a biofilm of thickness  $L_b$  is cultivated on a porous substrate of thickness  $L_p$ . The length of the system is  $l$ , which was equal to 60 mm in this study. The nutrient medium flows in the porous medium with superficial velocity  $u_p$  and in general can be driven by gravity, evaporation, or a pump. The chemical potential difference of species  $i$  between the porous medium and the biofilm drives the transport of nutrients to the cells. The photosynthetic biofilm is in direct contact with the gas phase at temperature  $T$  and pressure  $p$ , containing water vapor, carbon dioxide, and oxygen at partial pressures  $p_{\text{H}_2\text{O}}$ ,  $p_{\text{CO}_2}$ , and  $p_{\text{O}_2}$ , respectively. The biofilm is illuminated with uniform diffuse spectral irradiance  $G_{\lambda, \text{in}}$  as shown. The spatial coordinates  $x$  and  $y$  signify the distances from the origin in the in-plane and out-of-plane directions, respectively. The biofilm thickness and microorganism concentration were treated as constants for the duration of the simulation times as the time scale for photoautotrophic growth was much greater than the time scales for light and mass transport. For all simulations, it was assumed that the biomass concentration  $X$  was spatially homogeneous and equal to 100 kg dry weight per cubic meter ( $\text{kg DW}/\text{m}^3$ ).<sup>10</sup>

### Light transport model

**Assumptions.** In order to make light transport in the biofilm mathematically tractable, it was assumed that: (1) light

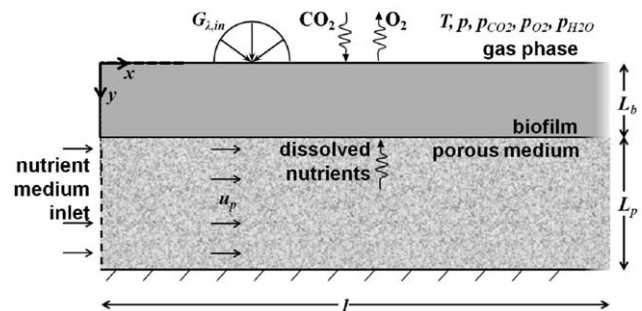


Figure 2. Schematic of the PSBR under analysis.



transport was one-dimensional and steady with respect to mass transport, (2) the medium surrounding the cells in the biofilm was non-emitting, weakly absorbing, and non-scattering in the photosynthetically active region (PAR) of the spectrum, and (3) independent scattering dominated over dependent scattering for the cell size parameters and volume fractions considered.<sup>25</sup>

**Governing Equations.** The local light availability is governed by the radiative transport equation (RTE). The one dimensional, spectral, steady-state RTE can be written as,<sup>25</sup>

$$\frac{\partial I_\lambda(y, \hat{s})}{\partial y} = -\kappa_{\text{eff}, \lambda} I_\lambda(y, \hat{s}) - \sigma_{\text{eff}, \lambda} I_\lambda(y, \hat{s}) + \frac{\sigma_{\text{eff}, \lambda}}{4\pi} \int_{4\pi} I_\lambda(y, \hat{s}_i) \Phi_\lambda(\hat{s}_i, \hat{s}) d\Omega_i \quad (1)$$

where  $I_\lambda(y, \hat{s})$  is the spectral radiant intensity at location  $y$  traveling in the direction  $\hat{s}$ , expressed in  $\text{W/m}^2 \text{ nm sr}$ . The parameters  $\kappa_{\text{eff}, \lambda}$  and  $\sigma_{\text{eff}, \lambda}$  are the effective absorption and scattering coefficients of the biofilm in  $\text{m}^{-1}$ , and can be written as,

$$\kappa_{\text{eff}, \lambda} = \kappa_{\text{m}, \lambda} (1 - vX) + A_{\text{abs}, \lambda} X \quad (2)$$

$$\sigma_{\text{eff}, \lambda} = S_{\text{sca}, \lambda} X \quad (3)$$

where  $X$  is the microorganism concentration and  $\kappa_{\text{m}, \lambda}$  is the absorption coefficient of the medium surrounding the cells, which was assumed to be equal to that of water. The spectral absorption coefficients of water can be written as,<sup>26</sup>

$$\kappa_{\text{m}, \lambda} = \frac{4\pi k_\lambda}{\lambda} \quad (4)$$

where  $k_\lambda$  is the absorption index of water reported by Hale and Querry.<sup>27</sup> In Eq. (2), the parameter  $v$  is the specific volume of the microorganisms, assumed to be equal to  $0.001 \text{ m}^3/\text{kg}$ .<sup>26</sup> The mass absorption and scattering cross sections,  $A_{\text{abs}}$  and  $S_{\text{sca}}$ , respectively, are both expressed in  $\text{m}^2/\text{kg}$  and were reported by Berberoglu and Pilon.<sup>28</sup>

Moreover, in Eq. (1),  $\Phi_\lambda$  is the scattering phase function, which is the probability that radiation traveling in the solid angle  $d\Omega_i$  around the direction  $\hat{s}_i$  will be scattered into the solid angle  $d\Omega$  around direction  $\hat{s}$ . The integral term in Eq. 1 accounts for the multiple scattering phenomena in a dense culture. The photosynthetically active irradiance,  $G_{\text{PAR}}$ , was defined as,<sup>25</sup>

$$G_{\text{PAR}}(y) = \int_{400 \text{ nm}}^{700 \text{ nm}} \int_{4\pi} I_\lambda(y, \hat{s}) d\Omega d\lambda \quad (5)$$

Finally, the optical thickness has been shown to be an appropriate parameter for scaling light availability in algae cultivation systems.<sup>22</sup> The local optical thickness  $\tau$  is the product of mass extinction coefficient,  $E_{\text{ext}}$ , the volumetric biomass concentration,  $X$ , and the physical distance from the light facing surface,  $y$ . The mass extinction cross section in the photosynthetically active region was reported to be  $355 \text{ m}^2/\text{kg}$  for *A. variabilis*.<sup>26</sup>

**Boundary Conditions.** The biofilm was illuminated with diffuse fluorescent lighting with a color temperature of 4100 K, the spectral content of which was reported by Murphy et al. at 10 nm resolution.<sup>24</sup> The boundary conditions for light intensity in the biofilm can be written as,

$$\begin{aligned} I_\lambda(y=0, \theta) &= (1-r_b)G_{\lambda, \text{in}}/\pi \quad \text{for } 0 \leq \theta \leq \pi/2 \\ I_\lambda(y=L_b, \theta) &= r_p G_\lambda^+(y=L_b)/\pi \quad \text{for } \pi/2 \leq \theta \leq \pi \end{aligned} \quad (6)$$

where  $\theta$  is the zenith angle with respect to the normal into the biofilm. The parameter  $G_\lambda^+$  is the spectral irradiance at the biofilm-porous medium interface in the direction into the porous medium. The parameters  $r_b$  and  $r_p$  represent the hemispherical-hemispherical reflectances of the biofilm and porous medium, and were equal to 0.04 and 0.5, respectively, in the PAR.<sup>29</sup>

**Solution Method and Grid Size Independence.** The RTE was solved numerically using the discrete ordinates method with a combination of two Gauss quadrature having 24 discrete directions per hemisphere along with the associated weighting factors successfully used by Baillis et al. for strongly forward media.<sup>28,30</sup> Convergence studies were performed to ensure that the computed values of  $G_\lambda(y)$  were independent of both the grid size and the angular discretization. To do so, the number of grid points was doubled until the relative discrepancy between  $G_\lambda(y)$  obtained for two consecutive grid refinements did not change by more than 1%. It was found that 240 points along the  $y$ -direction satisfied this criterion. Moreover, the values of  $G_\lambda(y)$  did not vary by more than 0.6% as the number of directions per hemisphere was increased from 24 to 30.<sup>28</sup>

### Mass transport model

**Assumptions.** To facilitate modeling of mass transport in the system, it was assumed that (1) advection in the out-of-plane direction was negligible in the biofilm and porous medium as the gas phase adjacent to the biofilm was saturated with water vapor, (2) the in-plane velocity, and hence in-plane advective transport in the biofilm was negligible, (3) the temperature, pressure, and partial pressures of  $\text{CO}_2$ ,  $\text{O}_2$ , and  $\text{H}_2\text{O}$  in the gas phase were actively maintained at constant values, and (4) the pH was uniform across the thickness of the biofilm. In reality, the pH in cyanobacterial films increases by as much as 0.0018 pH units per micron depth into the film due to carbon consumption.<sup>31–33</sup> The primary effects of the pH increase in the depth direction will be on speciation in the carbon system (from  $\text{H}_2\text{CO}_3$  to  $\text{HCO}_3^-$ ,  $\text{pK}_a$  6.3) and the phosphate system (from  $\text{H}_2\text{PO}_4^-$  to  $\text{HPO}_4^{2-}$ ,  $\text{pK}_a$  7.2).<sup>34</sup> However, in the pH range of 7.5 to 9.0 observed in these films, the fraction of carbon existing as bicarbonate ( $\text{HCO}_3^-$ ) is greater than 95% and is insensitive to a pH change of 0.18 units that would be expected in a 100  $\mu\text{m}$  biofilm.<sup>34</sup> Moreover, cells can uptake either  $\text{H}_2\text{PO}_4^-$  or  $\text{HPO}_4^{2-}$  to satisfy their phosphate requirement.<sup>35,36</sup> Thus, neglecting the pH variation in the depth direction is expected to have negligible effects on the predicted biofilm productivity.

**Governing Equations.** Given the above assumptions, the equation governing the concentration of nutrient  $i$  in the porous medium, denoted as  $[i]$ , can be written as,<sup>37</sup>

$$\frac{\partial [i]}{\partial t} = D_{i,p} \frac{\partial^2 [i]}{\partial y^2} + D_{i,p} \frac{\partial^2 [i]}{\partial x^2} - \frac{\partial}{\partial x} ([i]u_p) \quad (7)$$

where  $D_{i,p}$  is the diffusion coefficient of nutrient  $i$  in the porous medium. The left hand side of Eq. (7) accounts for storage of nutrient  $i$ . The first two terms on the right hand side account for diffusion in the out-of-plane and in-plane

**Table 1. Elemental Composition of 14 Cyanobacterial Strains and BG11 Nutrient Medium with Respect to Phosphorous Content**

Cyanobacterium	mol/mol P					
	N	P	K	Mg	S	Ca
<i>Synechococcus</i> (2 strains) <sup>40</sup>	29	1.0	–	–	–	–
<i>Synechococcus</i> (2 strains) <sup>41</sup>	14	1.0	–	–	–	–
<i>Prochlorococcus</i> (7 strains) <sup>40,41</sup>	20	1.0	–	–	–	–
<i>Anabaena flos-aquae</i> <sup>42</sup>	–	1.0	0.89	0.34	0.20	0.19
<i>Anabaena</i> sp. <sup>43</sup>	–	1.0	1.03	0.23	0.44	0.66
<i>Microcystis aeruginosa</i> <sup>44</sup>	–	1.0	0.91	0.58	0.52	0.79
Average	20	1.0	0.94	0.38	0.39	0.54
Standard deviation	8.0	0.0	0.08	0.18	0.17	0.32
BG11 <sup>23</sup>	77	1.0	2.00	1.33	1.33	1.07

directions, respectively, and the third term accounts for advection in the in-plane direction.

Similarly, the governing equation for mass transport in the biofilm can be written as,<sup>37</sup>

$$\frac{\partial[i]}{\partial t} = D_{i,b} \frac{\partial^2[i]}{\partial y^2} + D_{i,b} \frac{\partial^2[i]}{\partial x^2} - \gamma_i \quad (8)$$

where  $D_{i,b}$  is the diffusive permeability of species  $i$ , which is the appropriate parameter governing transport of solutes that are produced or consumed in biofilms, such as nutrients and molecular oxygen.<sup>38</sup> The consumption term  $\gamma_i$  can be written as,

$$\gamma_i = \frac{\mu X}{Y_{X/i}} \quad (9)$$

where  $\mu$  is the local growth rate, expressed in  $s^{-1}$ , and  $X$  is the biomass concentration in  $kg/m^3$ . The parameter  $Y_{X/i}$  is the biomass yield based on the amount of nutrient  $i$  consumed, expressed in g dry biomass/mol  $i$ .<sup>39</sup>

**Identification of Growth-Limiting Nutrient.** The nutrients whose availabilities were most likely to limit growth were identified. Table 1 compares the elemental compositions of 14 different cyanobacterial species to that of the nutrient medium BG11.<sup>23,40–44</sup> The table indicates that, from an elemental analysis perspective, cyanobacteria growing in BG11 will first exhaust the available phosphorous before exhausting any other macronutrient present therein. Moreover, it was evident that the micronutrients Fe, Mn, Zn, Mo, Cu, and Co would not be growth-limiting as BG11 is replete with these elements with respect to algal biomass composition.<sup>45</sup> Therefore, this study focused on the transport of phosphate through the reactor to identify locations of growth limitation by the limiting nutrient from the nutrient medium. Moreover, inorganic carbon transport was also considered because it is delivered from the gas phase rather than from the porous medium and can be a limiting factor in high cell density systems.<sup>46</sup> Finally, molecular oxygen transport was also modeled to identify locations of oxygen inhibition.<sup>47,48</sup>

**Growth Kinetic Model.** The local growth rate  $\mu$  was calculated using the Monod model taking into account limitation and inhibition for nutrients and irradiance, which can be written as,<sup>49</sup>

$$\mu = \mu_{\max} \left( \frac{G_{PAR}}{K_{S,G} + G_{PAR} + G_{PAR}^2/K_{I,G}} \right) \frac{C_T}{K_{S,C} + C_T + C_T^2/K_{I,C}} f_P \quad (10)$$

where  $\mu_{\max}$  is the maximum specific growth rate in  $s^{-1}$  and  $K_{S,G}$  and  $K_{I,G}$  are the half-saturation and inhibition constants for irradiance, respectively, expressed in  $W/m^2$ . The parameters  $K_{S,C}$  and  $K_{I,C}$  are the half-saturation and inhibition

constants for the dissolved inorganic carbon concentration  $C_T$ , given in mol/L. Moreover,  $f_P$  is the phosphate limitation factor. The phosphate required for biofilm growth can be of intracellular or extracellular origin, depending on the extracellular phosphate concentration and intracellular phosphate reserves.<sup>50–52</sup> The phosphate limitation factor associated with extracellular phosphate consumption was calculated using the Monod model as,

$$f_{P,e} = \frac{P_T}{K_{S,P} + P_T + P_T^2/K_{I,C}} \quad (11)$$

where  $P_T$  is the extracellular phosphate concentration and  $K_{S,P}$  and  $K_{I,C}$  are the half saturation and inhibition constants, respectively. On the other hand, the phosphate limitation factor associated with intracellular phosphate consumption was calculated using the Droop equation, given by,

$$f_{P,i} = \mu_{\max}^* (1 - k_q/Q_P) \quad (12)$$

where  $\mu_{\max}^*$  is a dimensionless factor that accounts for a decrease in the maximum growth rate when extracellular phosphate is unavailable,  $Q_P$  is the intracellular phosphate concentration, and  $k_q$  is the minimum intracellular phosphate concentration required for growth.<sup>51</sup> The phosphate limitation factor was defined as the maximum of the intracellular and extracellular limitation factors.

**Parameters for Growth Kinetics and Biomass Yield.** Table 2 shows the half-saturation and inhibition constants  $K_{S,i}$  and  $K_{I,i}$  for each nutrient considered. As molecular oxygen was not a nutrient but an inhibitor, it featured an inhibition constant but no half-saturation constant.<sup>48</sup> The table also presents the biomass yields based on consumption of each nutrient,  $Y_{X/i}$ . These yields assume a cyanobacterial stoichiometry of  $C_{159}H_{263}O_{63}N_{20}P_1K_{0.94}Mg_{0.38}S_{0.39}Ca_{0.54}$ .<sup>40–44,51,52</sup> Moreover, the maximum specific growth rate  $\mu_{\max}$  was  $4.2 \times 10^{-5} s^{-1}$  and the half-saturation and inhibition constants for irradiance,  $K_{S,G}$  and  $K_{I,G}$  were  $38 W/m^2$  and  $400 W/m^2$ , respectively.<sup>54,55</sup> Finally, the relative maximum growth rate and minimum intracellular phosphate mass fraction required for growth,  $\mu_{\max}^*$  and  $k_q$ , were 0.24 and 2.7 mg P/g DW.<sup>51</sup>

**Table 2. Transport Properties and Kinetic Constants for the Dominant Species of Inorganic Carbon and Phosphate, and Molecular Oxygen, in the pH Range of 7 to 10**

	C	P	O
Dominant species	$HCO_3^-$	$H_2PO_4^-/HPO_4^{2-}$	$O_2$
$K_{S,i}$ (mM) <sup>54,56</sup>	0.2	0.017	–
$K_{I,i}$ (mM) <sup>48,54</sup>	18	–	2.7
$Y_{X/i}$ (kg/kmol) <sup>51,54</sup>	22.4	1410	–
$D_{i,w}$ ( $m^2/s \times 10^{10}$ ) <sup>57,58</sup>	11.8	7.6/8.8	20.0
$D_{i,b}$ ( $m^2/s \times 10^{10}$ )	2.2	1.5/1.7	3.8
$D_{i,p}$ ( $m^2/s \times 10^{10}$ )	9.4	6.1/7.0	16.0

It should be noted that these growth kinetic constants and biomass stoichiometry were obtained from the literature for planktonic cultures, and as such, there is some uncertainty in their values when applied to microorganisms in biofilms. Therefore, a sensitivity analysis was performed to investigate the dependence of local growth rates on growth kinetic constants and biomass stoichiometry. For this, local growth rates were recorded when the half saturation and inhibition constants  $K_S$  and  $K_I$  for light and nutrients, the maximum specific growth rate  $\mu_{\max}$ , and the stoichiometric coefficient for phosphorous were varied from  $-50\%$  to  $+50\%$  of the values presented in Table 2.

**Diffusive Permeabilities of Nutrient Species.** Table 2 also shows the dominant species containing C and P in the pH range 7 to 10, along with their diffusion coefficients in the porous medium ( $D_{i,p}$ ) and their diffusive permeabilities in the biofilm ( $D_{i,b}$ ).<sup>34,57–59</sup> The relative effective diffusion coefficient of each species in the porous medium,  $D_{i,p}^*$ , was defined as its diffusion coefficient in the porous medium with respect to its diffusion coefficient in water. The value of  $D_{i,p}^*$  was assumed to be equal to 0.8 based on the results presented by Mu et al. and assuming a porous medium void fraction of 0.85.<sup>60</sup> Similarly, the relative effective diffusive permeability of species  $i$  in the biofilm,  $D_{i,b}^*$ , was calculated as,<sup>59</sup>

$$D_{i,b}^* = 1 - \frac{0.43X^{0.92}}{11.19 + 0.27X^{0.99}} \quad (13)$$

where  $X$  is the microorganism concentration, given in kg DW/m<sup>3</sup>.

**Initial Conditions.** The initial conditions corresponded to the biofilm and porous medium being in equilibrium with the gas phase and nutrient medium in the dark. The initial dissolved inorganic carbon concentration in the system,  $C_{i,T}$ , can therefore be written as,<sup>34</sup>

$$C_{i,T}(x, y, t=0) = p_{CO_2} K_{H,CO_2} \left( 1 + K_{a1} [H^+]^{-1} + K_{a1} K_{a2} [H^+]^{-2} \right) \quad (14)$$

where  $p_{CO_2}$  is the partial pressure of CO<sub>2</sub> in the gas phase, equal to 47 Pa, and  $K_{H,CO_2}$  is Henry's constant for aqueous CO<sub>2</sub> in equilibrium with the gas phase, equal to  $3.4 \times 10^{-7}$  M/Pa at 25°C.<sup>34</sup> Moreover,  $K_{a1}$  and  $K_{a2}$  are the first and second equilibrium constants for the carbonate system, equal to  $10^{-6.3}$  and  $10^{-10.3}$ , respectively, and  $[H^+]$  is the proton concentration, equal to  $10^{-pH}$ .<sup>34</sup> The three terms on the right hand side represent carbonic acid [ $H_2CO_3^*$ ], bicarbonate [ $HCO_3^-$ ], and carbonate [ $CO_3^{2-}$ ], respectively.

Similarly, the initial dissolved oxygen concentration was given by,<sup>34</sup>

$$[O_2](x, y, t=0) = p_{O_2} K_{H,O_2} \quad (15)$$

where  $p_{O_2}$  is the partial pressure of oxygen in the gas phase, equal to 21.3 kPa, and  $K_{H,O_2}$  is Henry's constant for aqueous oxygen in equilibrium with the gas phase, equal to  $1.3 \times 10^{-8}$  M/Pa at 25°C.<sup>34</sup> Thus, the initial oxygen concentration at all locations in the biofilm and the porous medium was  $2.7 \times 10^{-4}$  M.

The initial total inorganic phosphate concentration  $P_T$ , given by the sum of  $[H_2PO_4^-]$  and  $[HPO_4^{2-}]$ , were equal to their concentrations in fresh BG11 medium. The initial conditions for the phosphate concentration can therefore be written as,

$$P_T(x, y, t=0) = P_{T,o} \quad (16)$$

where  $P_{T,o}$  was equal to  $2.3 \times 10^{-4}$  M.<sup>23</sup>

**Boundary Conditions.** In PSBRs, inorganic carbon and molecular oxygen are exchanged directly with the gas phase adjacent to the biofilm, whereas all other dissolved nutrients are delivered from the porous medium side by the nutrient medium. Thus, the biofilm surface was taken to be in chemical equilibrium with the gas phase at all times. Moreover, a zero flux boundary condition was imposed at the interface between the porous medium and the impermeable wall supporting it. Therefore, the boundary conditions for the total inorganic carbon concentration can be written as,<sup>34</sup>

$$C_{i,T}(x, y=0, t) = p_{CO_2} K_{H,CO_2} \left( 1 + K_{a1} [H^+]^{-1} + K_{a1} K_{a2} [H^+]^{-2} \right) \quad (17)$$

$$\frac{\partial C_{i,T}}{\partial y}(x, y=L_b+L_p, t) = 0 \quad (18)$$

Similarly, the boundary conditions for the molecular oxygen concentration can be written as,<sup>34</sup>

$$[O_2](x, y=0, t) = p_{O_2} K_{H,O_2} \quad (19)$$

$$\frac{\partial [O_2]}{\partial y}(x, y=L_b+L_p, t) = 0 \quad (20)$$

For total phosphate, there was a zero flux boundary condition at the interface between the biofilm and the gas phase and at the interface between the porous medium and the solid supporting wall, which can be written as,

$$\frac{\partial P_T}{\partial y}(x, y=0, t) = 0 \quad (21)$$

$$\frac{\partial P_T}{\partial y}(x, y=L_p+L_b, t) = 0 \quad (22)$$

Moreover, the phosphate concentration at the nutrient medium inlet was equal to its concentration in fresh BG11,  $P_{T,o}$ , which can be written as,

$$P_T(x=0, y, t) = P_{T,o} \quad (23)$$

**Solution Method and Grid Size Independence.** The transient, explicit discretization method was used to solve Eqs. (7) to 10 simultaneously.<sup>61</sup> Moreover, the pH at each location was calculated taking into account the local nutrient medium composition and the partial pressure of CO<sub>2</sub> using the software package Visual Minteq.<sup>62</sup> The system was deemed to be at steady state when the percent rate of change of the concentrations of all nutrients were less than 0.01% per second. Convergence studies were performed to ensure that the computed nutrient concentrations and growth rates were independent of spatial and temporal discretization. To do so, the discretization size in the in-plane and out-of-plane directions as well as the time step size were decreased until the relative discrepancy between the local growth rates obtained for two consecutive grid refinements did not change by more than 1%. This criterion was satisfied for a discretization scheme consisting of 10 nodes in the out-of-plane direction in each the biofilm and the porous medium, 10 nodes in the in-plane direction, and a time step of 0.05 s.

#### Nutrient delivery metrics

To identify the specific causes of suboptimal local growth rates, the local delivery effectiveness for nutrient  $i$ ,  $\eta_{d,i}$ , was



defined as the ratio of the local growth rate to the growth rate that would exist with no limitation or inhibition by nutrient  $i$ . For oxygen, the parameter  $\eta$  was defined as the removal effectiveness rather than the delivery effectiveness as oxygen is inhibitory to growth. Moreover, the phosphate delivery effectiveness took into account only the extracellular phosphate concentration, and is given by Eq. (11).

## Results and Discussion

### Experimental PSBR performance

Figure 3 shows the experimentally measured biomass production rates of three PSBRs. The initial biofilm thicknesses in reactors 1, 2, and 3 were 45  $\mu\text{m}$ , 35  $\mu\text{m}$ , and 41  $\mu\text{m}$ , respectively. Moreover, the nutrient medium velocities through the porous strips were 25  $\mu\text{m/s}$ , 12  $\mu\text{m/s}$ , and 3.3  $\mu\text{m/s}$ , respectively. Error bars on the experimental data represent the standard error from the duplicate experiments. The biomass production rate at a downstream distance of 0.5 cm was directly related to the initial biofilm thickness, as the 35  $\mu\text{m}$  thick biofilm had a biomass production rate of 0.09  $\text{g/m}^2 \text{ hr}$  at this location, whereas the two thicker biofilms had a biomass production rate of 0.12  $\text{g/m}^2 \text{ hr}$ . In all three reactors, the biomass production rate decreased in the direction of nutrient medium flow, which is attributed to upstream nutrient consumption. For the range spanning from 0 to 4 cm from the nutrient medium inlet, the slopes of the biomass production rate versus distance from the inlet for reactors 1, 2, and 3 were  $-0.013$ ,  $-0.007$ , and  $-0.026 \text{ g/m}^2 \text{ hr cm}$ , respectively. Furthermore, this decline was more gradual in the range spanning from 4 to 6 cm from the inlet, as the rates of decline in this region were  $-0.006$ ,  $-0.003$ , and  $-0.003 \text{ g/m}^2 \text{ hr cm}$ , respectively. The more gradual decline at farther distances from the nutrient medium inlet is attributed to a regime change from extracellular to intracellular phosphate consumption.

The total photosynthetic efficiencies of the experimental biofilms, defined as the total rate of energy storage in the growing biomass divided by the incident light energy, were 2.8%, 1.9%, and 2.3%, respectively. By comparison, photosynthetic efficiencies of open ponds, tubular photobioreactors, and planar photobioreactors are about 1.5%, 3%, and

5%, respectively.<sup>63</sup> The following sections investigate strategies for enhancing photosynthetic productivity of PSBRs.

### Biofilm growth rate without nutrient limitation or inhibition

The local growth rates in the biofilm were calculated taking into account only the local irradiance, assuming no nutrient limitation or inhibition. This maximum photon utilization case serves as a benchmark for evaluating mass transport limited growth rates.

Figure 4 shows the local photosynthetically active irradiance as well as the local growth rates assuming no nutrient limitation or inhibition within biofilms of thickness 20  $\mu\text{m}$ , 100  $\mu\text{m}$ , and 200  $\mu\text{m}$ , irradiated at 20 and 200  $\text{W/m}^2 \text{ PAR}$ , as functions of local optical thickness  $\tau$ . At 20  $\text{W/m}^2 \text{ irradiance}$ , all three biofilms displayed a light limited regime at the illuminated surface where the maximum growth rate was 0.095  $\text{h}^{-1}$ . On the other hand, at 200  $\text{W/m}^2 \text{ irradiance}$ , the biofilm was light inhibited from the illuminated surface up to an optical depth of 0.6 at which the maximum growth rate of 0.11  $\text{h}^{-1}$  was reached.

Additionally, Figure 5 shows the total biomass production rates of the biofilms of thickness 20  $\mu\text{m}$ , 100  $\mu\text{m}$ , and 200  $\mu\text{m}$  as functions of incident irradiances ranging from 0 to 400  $\text{W/m}^2 \text{ PAR}$ , which is the range expected for systems using natural sunlight. For the 100  $\mu\text{m}$  and 200  $\mu\text{m}$  thick biofilms, the total biomass production rate increased monotonically with increasing incident irradiance, and maximum biomass production rates of 0.95 and 1.2  $\text{g/m}^2 \text{ hr}$ , respectively, occurred at the maximum irradiance of 400  $\text{W/m}^2 \text{ PAR}$ . On the other hand, the maximum total biomass production rate for the 20  $\mu\text{m}$  thick biofilm of 0.22  $\text{g/m}^2 \text{ hr}$  occurred at an incident irradiance of 200  $\text{W/m}^2 \text{ PAR}$ . At irradiances greater than 200  $\text{W/m}^2 \text{ PAR}$ , every cell within 20  $\mu\text{m}$  of the surface was photoinhibited. Cells within 20  $\mu\text{m}$  of the surface in the 100  $\mu\text{m}$  and 200  $\mu\text{m}$  thick biofilms were also photoinhibited, but cells farther from the surface were photolimited, and therefore the overall effect of increasing the irradiance onto these biofilms was an increase in total biofilm productivity.

### Numerical model parameter fitting

Due to availability in the literature, the growth kinetic parameters and biomass stoichiometries for planktonic cyanobacterial cultures were used for initial biofilm growth rate modeling. However, it was plausible that these parameters would be different for cells growing in biofilms than for planktonic cultures. Therefore, a sensitivity analysis was performed to investigate the dependence of local growth rates in the biofilm on the growth kinetic parameters and biomass stoichiometries. It was determined that the local growth rates were most sensitive to the maximum specific growth rates corresponding to extracellular and intracellular phosphate consumption,  $\mu_{\text{max}}$  and  $\mu_{\text{max}}^*$ , and the biomass yield based on phosphate consumption  $Y_{X/P}$ . Therefore, these parameters were varied to match the numerical and experimental results.

Figure 6 shows the numerically predicted biomass production rates as a function of distance from the nutrient medium inlet, alongside the experimental results. For these simulations, the cells' intracellular phosphate concentration,  $Q_P$ , was equal to  $7.1 \times 10^{-4} \text{ mol P/g DW}$  due to their exposure to fresh BG11 while growing on the floating bioreactors

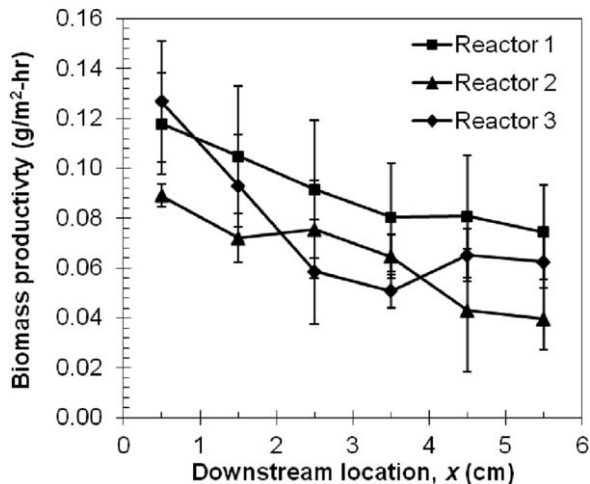


Figure 3. Results from the productivity monitoring experiments for reactor 1 (thickness  $L_b$  45  $\mu\text{m}$ , nutrient medium velocity  $u_p$  25  $\mu\text{m/s}$ ), reactor 2 ( $L_b$  35  $\mu\text{m}$ ,  $u_p$  12  $\mu\text{m/s}$ ), and reactor 3 ( $L_b$  41  $\mu\text{m}$ ,  $u_p$  3.3  $\mu\text{m/s}$ ).

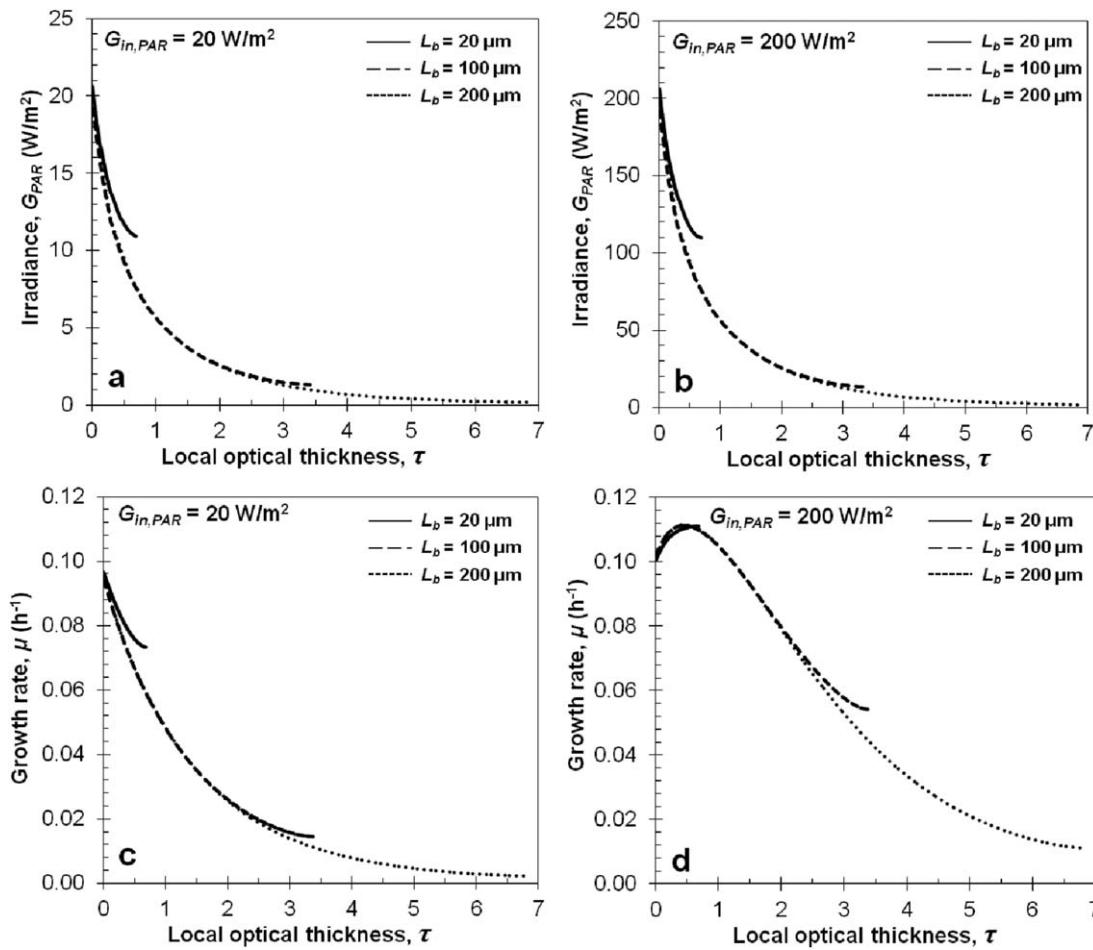


Figure 4. (a and b) Local photosynthetically active irradiance as a function of local optical thickness for an incident irradiance of 20 W/m<sup>2</sup> and 200 W/m<sup>2</sup> PAR, and (c and d) local growth rate with no nutrient limitation or inhibition for incident irradiances of 20 W/m<sup>2</sup> and 200 W/m<sup>2</sup> PAR.

prior to operating as PSBRs. This value was selected based on the results presented by Riegman and Mur (1984), which showed that cyanobacterial cells attained this intracellular phosphate concentration when exposed to nutrient medium with phosphate concentrations comparable to that of BG11.<sup>51</sup>

Figure 6 indicates that the model predicted local growth rates in reactors 1, 2, and 3 with average percent errors of 13%, 16%, and 8%, respectively. Moreover, the values for  $\mu_{max}$ ,  $\mu_{max}^*$ , and  $Y_{X/P}$  were 0.18 h<sup>-1</sup>, 0.56, and 4,280 g DW/mol P, respectively. By comparison, the initially used values for these parameters were 0.15 h<sup>-1</sup>, 0.24, and 3,570 g DW/mol P, respectively.

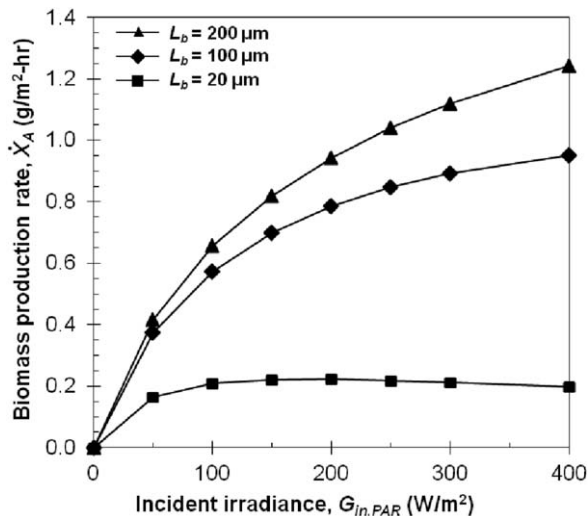


Figure 5. Total biomass production rate as a function of incident photosynthetically active irradiance for biofilm thicknesses of 20  $\mu$ m, 100  $\mu$ m, and 200  $\mu$ m.

#### Flux balancing of nutrients and photons

It was observed numerically and experimentally that increasing the nutrient medium velocity through the porous medium caused a more gradual decline in biomass production rate with downstream distance. It is currently of interest to identify the mechanism for this decline and then provide design guidelines for balancing the fluxes of nutrients and photons for maximizing PSBR productivity.

Reactor 2 was chosen as an exemplary case to show the spatial distribution of growth rate and dissolved nutrient concentrations. Figure 7 shows the numerical results for local growth rates, as well as the concentrations of inorganic carbon, molecular oxygen, and extracellular phosphate for reactor 2, which featured a biofilm 35  $\mu$ m thick, exposed to a nutrient medium flow of 12  $\mu$ m/s. The figure indicates that the growth rate decreased exponentially with increasing distance from the illuminated surface due to light limitation.



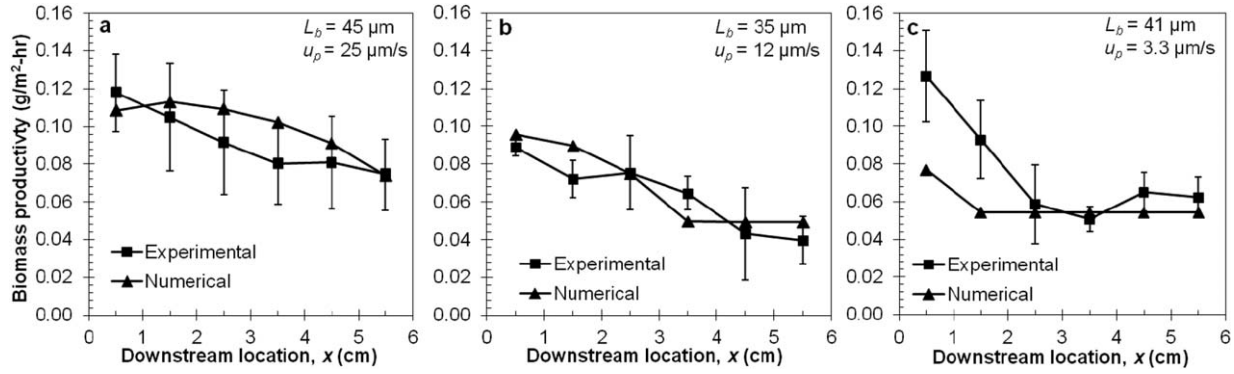


Figure 6. Comparison between numerical and experimental biomass production rates for (a) reactor 1, (b) reactor 2, and (c) reactor 3.

Moreover, the growth rate decreased in the direction of flow at a rate of about  $0.11 \text{ g/m}^2 \text{ hr mm}$ .

To elucidate the cause of the declining growth rate in the flow direction, Figure 8 shows the local delivery/removal effectivenesses of total carbon, oxygen, and total phosphate in the biofilm. The figure indicates that the minimum values of  $\eta_{d,C_T}$  and  $\eta_{r,O_2}$  in the biofilm were 0.93 and 0.89, respectively, whereas the phosphate delivery effectiveness decreased to 0.5 at a location 3 cm from the nutrient medium inlet. At locations greater than 3.5 cm from the nutrient medium inlet, stored intracellular phosphate was used for growth. For long-term operation, nutrients should be provided to the cells at the rate at which they are consumed for growth, rather than relying on intracellular reserves. Therefore, the phosphate delivery length,  $x_{PD}$  was defined as the distance from the nutrient medium inlet at which the phosphate delivery effectiveness decreased to 0.5. The phosphate delivery lengths for reactors 1, 2, and 3 based on the numerical simulations were 6 cm, 3.5 cm, and 0.7

cm, respectively. For efficient nutrient utilization and biofilm growth, the of the phosphate delivery length should be matched to the physical length of the biofilm in the flow direction.

*Scaling Analysis for Nutrient Delivery Enhancement.* To develop a generalized strategy for mitigating inadequate nutrient delivery, a scaling analysis was performed in which the nutrient delivery rate into the porous medium was compared to the nutrient consumption rate by the biofilm. Neglecting diffusion in the in-plane direction in the porous medium yields the relationship,

$$u_p L_p [i_L]_o \sim \frac{\mu_o X L_b}{Y_{X/i_L}} x_{iD} \quad (24)$$

where the left and right hand sides represent the transport and consumption rates, respectively, of the growth-limiting nutrient  $i_L$ , which is phosphate in the current study. The parameters  $[i_L]_o$  and  $\mu_o$  represent the concentration of the growth-limiting nutrient and the thickness-averaged growth rate, respectively, at the nutrient medium inlet.

Rearranging Eq. (24) for the phosphate delivery length  $x_{PD}$  yields,

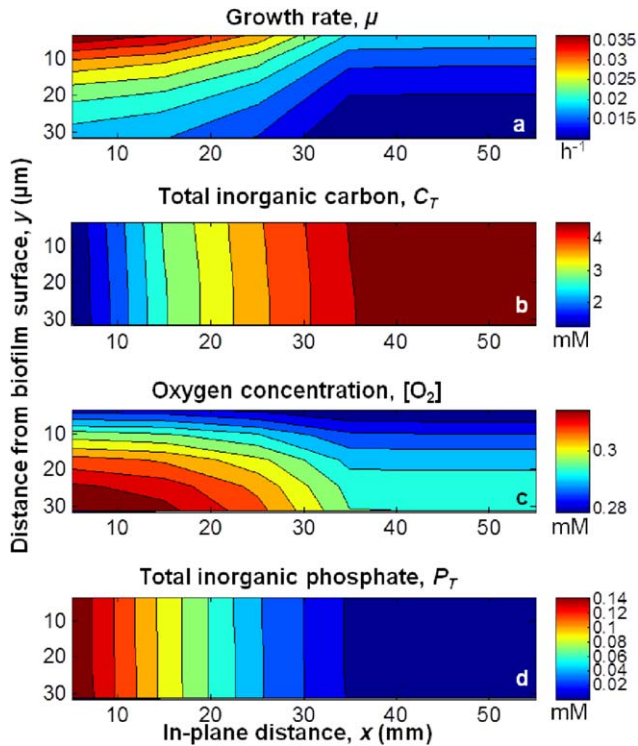


Figure 7. Local (a) growth rate, and concentrations of (b) total inorganic carbon, (c) molecular oxygen, and (d) phosphate for the numerical simulation of reactor 2.

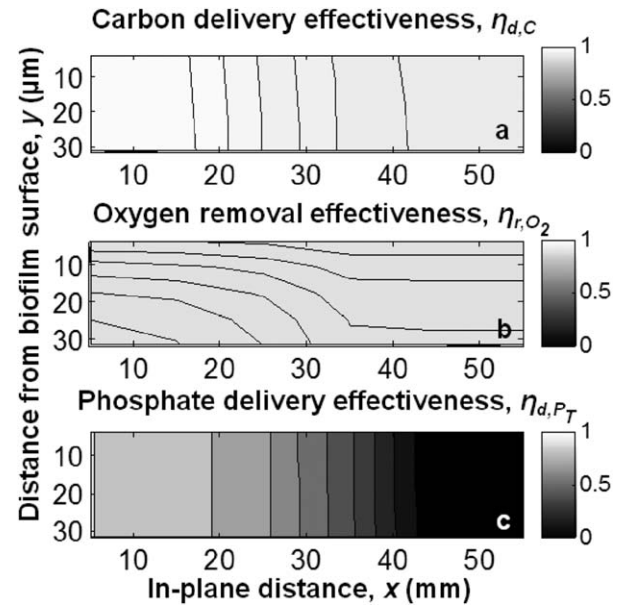


Figure 8. (a) Carbon delivery effectiveness, (b) oxygen removal effectiveness, and (c) phosphate delivery effectiveness for the biofilm of reactor 2.

$$x_{PD} = C \frac{\mu_p L_p [i_{L_0}] Y_{X/i_L}}{\mu_0 X L_b} \quad (25)$$

where  $C$  is a constant of proportionality based on Monod kinetics. Using the nutrient medium velocities, biomass production rates, and phosphate delivery lengths for the three experimental reactors yields a  $C$  value of 0.2. Equation (25) enables PSBRs to be designed such that the rate of nutrient delivery is matched to the rate of nutrient consumption. The phosphate delivery length can be manipulated by controlling the irradiance onto the biofilm, the biofilm thickness, the nutrient medium flow velocity, and the concentration of the limiting nutrient in fresh nutrient medium.

### Implications for scaled up PSBRs

The reactor used in the experimental part of this study was specially constructed for the laboratory scale in that it enabled precise control of the gas phase surrounding the biofilm and real time biofilm monitoring. A scaled up PSBR, on the other hand, typically consists of multiple parallel vertical porous substrates, all of which host biofilm growth.<sup>5,13,14</sup> Such a reactor type is advantageous over a single horizontal porous substrate because its high specific surface area increases the biomass per footprint area and decreases the irradiance onto each biofilm, mitigating photoinhibition. From geometric arguments, the average irradiance onto each biofilm in a scaled up PSBR is equal to  $G_{in}s/2h$ , where  $G_{in}$  is the irradiance incident onto the top horizontal surface of the reactor,  $s$  is the distance between adjacent plates, and  $h$  is the plate height. It is currently of interest to estimate the productivity of a scaled up outdoor PSBR using the experimental results obtained in this study. The biofilm of reactor 1, the most productive of the three reactors, exhibited a productivity based on biofilm area of  $0.09 \text{ g/m}^2 \text{ hr}$  under an irradiance of  $24 \text{ W/m}^2 \text{ PAR}$ . Under full sunlight of  $400 \text{ W/m}^2 \text{ PAR}$ , an average irradiance onto each biofilm of  $24 \text{ W/m}^2$  can be accomplished using a spacing aspect ratio  $s/h$  of 0.12, which corresponds to a biofilm to footprint area ratio of 17. Assuming uniform diffusion of the incident radiation, the scaled up reactor would have a productivity based on footprint area of about  $1.5 \text{ g/m}^2 \text{ hr}$  under full sunlight. Further assuming a sinusoidal distribution of irradiance over the course of a 14-h day yields a daily productivity of  $14 \text{ g/m}^2 \text{ day}$ , which is competitive with conventional open ponds and closed photobioreactors, which have productivities of about 11 and  $27 \text{ g/m}^2 \text{ day}$ , respectively.<sup>15</sup> Compared with these planktonic reactors, PSBRs have the advantage of high biomass density, which decreases the energy required for transporting water through the system as well as dewatering the biomass.

For efficient operation and nutrient utilization in scaled up PSBRs, the phosphate delivery length and physical length of the biofilm in the flow direction should be of equal scale. The phosphate delivery length is in turn a function of the nutrient medium flow rate and composition, as well as the microorganism density and irradiance. In evaporation driven PSBRs, the flow rate is equal to the evaporation rate from the terminal porous end, which is in turn the product of the surface area of the terminal end and the evaporative flux from it. The evaporative flux can be increased by blowing air past the terminal ends or actively or passively heating them. Moreover, the terminal ends of a scaled up evaporation driven PSBR protrude vertically into the ambient air,<sup>5</sup> and the flow rate through each porous substrate can therefore be increased by increasing the height of the exposed end.

However, increasing the height of the terminal end also causes shading of the biofilms, and it can potentially create a humid air zone between adjacent plates, thus decreasing the evaporative flux. There is also a maximum flow rate through the substrate that corresponds to the balance between capillary pressure at the air-water interface and the sum of the gravitational and viscous pressure drops in the flow direction.<sup>64</sup> For example, we estimated that the maximum flow velocity through a glass fiber porous substrate of an evaporation driven PSBR was approximately  $50 \text{ } \mu\text{m/s}$ . For *A. variabilis* grown with BG11 under an irradiance of  $24 \text{ W/m}^2$ , this velocity corresponds to a phosphate delivery length of about 10 cm. Therefore, 10 cm provides an upper bound for the height of evaporation driven PSBRs.

Furthermore, unless a water vapor reclamation system is employed, operation of evaporation driven PSBRs requires water loss from the reactor. If waste, sea, or brackish water is used for operation, this water loss may be acceptable at large scale. However, the value of water must be taken into account when designing scaled up PSBRs.

The phosphate delivery length can also be increased by increasing the phosphate concentration in fresh nutrient medium. However, this concentration can only be increased to a critical value, at which point another nutrient will become growth-limiting. For the example of cultivating cyanobacteria with BG11, when the phosphate concentration in fresh medium is doubled, calcium becomes limiting to growth (Table 1). To address this challenge, custom nutrient medium can be engineered that matches the elemental composition of the organism being cultivated, a strategy which has been successfully applied to suspended cultivation of green algae.<sup>65,66</sup> Moreover, such an engineered nutrient medium can be used in concentrated form to increase the phosphate delivery length while maintaining a constant flow velocity. However, precipitation of calcium phosphate and other possible solids within the porous medium as well as adverse effects of altered pH on microorganism productivity must carefully be taken into account.

### Conclusions

This article reported a combined experimental and numerical study on the operation and design of Porous Substrate Bioreactors. A comprehensive model integrating light transport, mass transport, and algal growth kinetics was constructed for understanding the effects of nutrient and photon delivery on the productivity of photosynthetic biofilms. Experimental data for the spatial dependence of biomass production rate of the cyanobacterium *Anabaena variabilis* in this reactor type was used to inform the model. It was observed that the biofilm growth rate declined in the direction of nutrient medium flow. A scaling parameter, termed the phosphate delivery length, was defined to guide design Porous Substrate Bioreactors for balancing the rate of nutrient delivery with the rate of nutrient consumption dictated by the photon flux. The model reported serves as a numerical tool for designing and optimizing the operating parameters of photosynthetic biofilm based cultivation systems.

### Nomenclature

- $A_{\text{abs}}$  = Mass absorption cross section,  $\text{m}^2/\text{kg}$
- $C_{i,T}$  = Total dissolved inorganic carbon,  $\text{mol/L}$
- $D_{i,j}$  = Diffusion coefficient or diffusive permeability of species  $i$  in species  $j$ ,  $\text{m}^2/\text{s}$

$D_{ij}^*$  = Relative diffusion coefficient or diffusive permeability of species  $i$  in species  $j$   
 $E_{\text{ext}}$  = Mass extinction cross section,  $\text{m}^2/\text{kg}$   
 $G$  = Irradiance,  $\text{W}/\text{m}^2$   
 $I_\lambda$  = Spectral radiant intensity,  $\text{W}/\text{m}^2 \text{ nm sr}$   
 $[i]$  = Concentration of species  $i$ ,  $\text{mol}/\text{L}$   
 $K$  = Constant for Monod model,  $\text{W}/\text{m}^2$  or  $\text{mol}/\text{L}$   
 $K_a$  = Equilibrium constant for carbonate system,  $\text{mol}/\text{L}$   
 $K_{H,i}$  = Henry's constant for species  $i$  in water,  $\text{mol}/\text{L Pa}$   
 $k$  = Absorption index  
 $L$  = Thickness,  $\text{m}$   
 $l$  = Length of the system,  $\text{m}$   
 $p$  = Pressure,  $\text{Pa}$   
 $P_T$  = Total dissolved inorganic phosphate,  $\text{mol}/\text{L}$   
 $r$  = Reflectance  
 $S_{\text{sca}}$  = Mass scattering cross section,  $\text{m}^2/\text{kg}$   
 $T$  = Temperature,  $^\circ\text{C}$   
 $t$  = Time,  $\text{s}$   
 $u_p$  = Superficial in-plane velocity,  $\text{m}/\text{s}$   
 $X$  = Microorganism concentration,  $\text{kg dry weight (DW)}/\text{m}^3$   
 $\dot{X}_A$  = Rate of areal biomass concentration increase,  $\text{kg}/\text{m}^2 \text{ s}$   
 $x$  = Dimension in the direction of nutrient medium flow,  $\text{m}$   
 $x_{\text{PD}}$  = Phosphate delivery length,  $\text{m}$   
 $Y_{X/i}$  = Biomass yield based on amount of  $i$  consumed,  $\text{kg DW}/\text{kmol } i$   
 $y$  = Dimension perpendicular to nutrient medium flow,  $\text{m}$

### Greek symbols

$\gamma$  = Consumption rate,  $\text{mol}/\text{L s}$   
 $\eta_{d/r}$  = Delivery/removal effectiveness  
 $\theta$  = Zenith angle,  $\text{rad}$   
 $\kappa$  = Absorption coefficient,  $\text{m}^{-1}$   
 $\lambda$  = Wavelength,  $\text{nm}$   
 $\mu$  = Growth rate,  $\text{s}^{-1}$   
 $v$  = Specific volume,  $\text{m}^3/\text{kg}$   
 $\sigma$  = Scattering coefficient,  $\text{m}^{-1}$   
 $\tau$  = Local optical thickness  
 $\Phi$  = Scattering phase function  
 $\Omega$  = Solid angle,  $\text{sr}$

### Subscripts

b = Refers to biofilm  
 I = Refers to inhibition  
 i = Refers to nutrient species  $i$   
 in = Refers to incident  
 m = Refers to medium  
 max = Refers to maximum  
 o = Refers to the nutrient medium inlet  
 p = Refers to porous medium  
 S = Refers to half-saturation

### Abbreviations

PAR = Photosynthetically active radiation  
 RTE = Radiative transport equation

### Acknowledgment

This study is based upon work supported by the National Science Foundation under Grant No. CBET-1125755. Any opinions, findings, and conclusions or recommendations expressed in this material are those of the authors and do not necessarily reflect the views of the National Science Foundation. The authors also thank Keith Macon for his help in the

multispectral image analysis method for biomass quantification. Moreover, the authors thank Begum Baysan for finding and summarizing many of the articles cited in this work. Finally, the authors thank two anonymous reviewers for their helpful comments and questions on the article.

### Literature Cited

- Li Y, Zhou W, Hu B, Min M, Chen P, Ruan RR. Integration of algae cultivation as biodiesel production feedstock with municipal wastewater treatment: strains screening and significance evaluation of environmental factors. *Bioresource Technol.* 2011; 102:10861–10867.
- Chisti Y. Biodiesel from algae. *Biotechnol Adv.* 2007;25:294–306.
- Pulz O, Gross W. Valuable products from biotechnology of microalgae. *Appl Microbiol Biol.* 2004;65:635–648.
- Demirbas A. Use of algae as biofuel sources. *Energy Convers Manage.* 2010;51:2738–2749.
- Murphy T, Fleming E, Bebout L, Bebout B, Berberoglu H. A novel microbial cultivation platform for space applications. In: *1st Annual International Space Station Research and Development Conference*. Denver, CO: American Astronomical Society (AAS); 2012, AAS 12-758.
- Borowitzka MA. Commercial production of microalgae: ponds, tanks, tubes, and fermenters. *J Biotechnol.* 1999;70:313–321.
- Singh RN, Sharma S. Development of suitable photobioreactor for algae production: a review. *Renewable Sustainable Energy Rev.* 2012;16:2347–2353.
- Beal CM, Hebner RE, Webber ME, Ruoff RS, Seibert AF. The energy return on investment for algal biocrude: results for a research production facility *Bioenergy Res.* 2011;5:341–362.
- Clarens AF, Resurreccion EP, White MA, Colosi LM. Environmental life cycle comparison of algae to other bioenergy feedstocks. *Environ Sci Technol.* 2010;44:1813–1819.
- Ozkan A, Kinney K, Katz L, Berberoglu H. Reduction of water and energy requirement of algae cultivation using an algae biofilm photobioreactor. *Bioresource Technol.* 2012;114:542–548.
- Liao Q, Wang Y-J, Wang Y-Z, Zhu X, Tian X, Li J. Formation and hydrogen production of photosynthetic bacterial biofilm under various illumination conditions. *Bioresource Technol.* 2010;101:5315–5324.
- Silva-Aciares FR, Riquelme CE. Comparisons of the growth of six diatom species between two configurations of photobioreactors. *Aquacult Eng.* 2008;38:26–35.
- Liu T, Wang J, Hu Q, Cheng P, Ji B, Liu J, Chen Y, Zhang W, Chen X, Chen L, Gao L, Ji C, Wang H. Attached cultivation technology of microalgae for efficient biomass feedstock production. *Bioresource Technol.* 2013;127:216–222.
- Naumann T, Cebi Z, Podola B, Melkonian M. Growing microalgae as aquaculture feeds on twin-layers, a novel solid state photobioreactor. *J Appl Phycol.* 2013;25:1413–1420.
- Jorquera O, Kiperstok A, Sales EA, Embiruçu M, Ghirardi ML. Comparative energy life-cycle analyses of microalgal biomass production in open ponds and photobioreactors. *Bioresource Technol.* 2010;101:1406–1413.
- Wanner O, Eberl H, Morgenroth E, Noguera D, Picioreanu C, Rittman B, van Loosdrecht M. *Mathematical Modeling of Biofilms*. London: IWA Publishing; 2006.
- Noguera DR, Okabe S, Picioreanu C. Review on biofilm modeling: present status and future directions. *Water Sci Technol.* 1999;39:273–278.
- Lewandowski Z, Beyenal H. *Fundamentals of Biofilm Research*. Boca Raton, FL: Taylor & Francis Group; 2007.
- Liao Q, Wang Y-J, Wang Y-Z, Chen R, Zhu X, Pu Y-K. Two-dimension mathematical modeling of photosynthetic bacterial biofilm growth and formation. *Int J Hydrogen Energy* 2012;37: 15607–15615.
- Yang Y, Liao Q, Zhu X, Wang H, Wu R, Lee D-J. Lattice Boltzmann simulation of substrate flow past a cylinder with PSB biofilm for bio-hydrogen production. *Int J Hydrogen Energy* 2011;36:14031–14040.
- Picioreanu C, Loosdrecht MCM, Heijnen JJ. Mathematical modeling of biofilm structure with a hybrid differential-discrete cellular automaton approach. *Biotechnol Bioeng.* 1998;58:101–116.



22. Murphy T, Berberoglu H. Effect of algae pigmentation on photobioreactor productivity and scale-up: a light transfer perspective. *J Quant Spectrosc Radiative Transfer* 2011;112:2826–2834.
23. Stanier RY, Kunisawa R, Mandel M, Cohen-Bazire G. Purification and properties of unicellular blue-green algae (order Chroococcales). *Bacteriol Rev.* 1971;35:171–205.
24. Murphy TE, Macon K, Berberoglu H. Multispectral image analysis for algal biomass quantification. *Biotechnol Progr.* 2013;29:808–816.
25. Siegel R, Howell J. *Thermal Radiation Heat Transfer*, 4th ed. New York: Taylor & Francis. 2002.
26. Berberoglu H, Pilon L. Experimental measurements of the radiation characteristics of *Anabaena variabilis* ATCC 29413-U and *Rhodospira rubra* ATCC 49419. *Int J Hydrogen Energy* 2007;32:4772–4785.
27. Hale GM, Querry MR. Optical constants of water in the 200-nm to 2000-nm wavelength region. *Appl Optics* 1973;12:555–563.
28. Berberoglu H, Pilon L. Maximizing the solar to H<sub>2</sub> energy conversion efficiency of outdoor photobioreactors using mixed cultures. *Int J Hydrogen Energy* 2010;35:500–510.
29. Kazemipour F, Méléder V, Launeau P. Optical properties of microphytobenthic biofilms (MPBOM): Biomass retrieval implication. *J Quant Spectrosc Radiative Transfer* 2011;112:131–142.
30. Baillis D, Pilon L, Randrianalisoa H, Gomez R, Viskanta R. Measurements of radiation characteristics of fused quartz containing bubbles. *J Opt Soc Am.* 2004;21:149–159.
31. Nakamura Y, Satoh H, Okabe S, Watanabe Y. Photosynthesis in sediments determined at high spatial resolution by the use of microelectrodes. *Water Res.* 2004;38:2439–2447.
32. Revsbech NP, Jørgensen BB, Blackburn TH, Cohen Y. Microelectrode studies of the photosynthesis and O<sub>2</sub>, H<sub>2</sub>S, and pH profiles of a microbial mat. *Limnol Oceanogr.* 1983;28:1062–1074.
33. Albertano P, Bruno L, Ottavi DD, Moscone D, Palleschi G. Effect of photosynthesis on pH variation in cyanobacterial biofilms from Roman catacombs. *J Appl Phycol.* 2000;12:379–384.
34. Morel FMM, Hering JG. *Principles and Applications of Aquatic Chemistry*. Hoboken, NJ: John Wiley & Sons; 1993.
35. Thiel T. Phosphate transport and arsenate resistance in the cyanobacterium *Anabaena variabilis*. *J Bacteriol.* 1988;170:1143–1147.
36. Isanovics V, Shafik HM, Presing M, Juhos S. Growth and phosphate uptake kinetics of the cyanobacterium, *Cylindrospermopsis raciborskii* (Cyanophyceae) in throughflow cultures *Freshwater Biol.* 2000;43:257–275.
37. Mills AF. *Mass Transfer*. Upper Saddle River, NJ: Prentice-Hall; 2001.
38. Stewart PS. A review of experimental measurements of effective diffusive permeabilities and effective diffusion coefficients in biofilms. *Biotechnol Bioeng.* 1999;34:261–272.
39. Dunn I, Heinzel E, Ingham J, Prenosil J. *Biological Reaction Engineering: Dynamic Modelling Fundamentals with Simulation Examples*, 2nd ed. Germany: Wiley-VCH; 2003.
40. Bertilsson S, Berglund O, Karl DM, Chisholm SW. Elemental composition of marine *Prochlorococcus* and *Synechococcus*: Implications for the ecological stoichiometry of the sea. *Limnol Oceanogr.* 2003;48:1721–1731.
41. Heldal M, Scanlan J, Norland S, Thingstad F, Mann NH. Elemental composition of single cells of various strains of marine *Prochlorococcus* and *Synechococcus* using X-ray microanalysis. *Limnol Oceanogr.* 2003;48:1732–1743.
42. Sigeo DC, Teper J, Levado E. Elemental composition of the cyanobacterium *Anabaena flos-aquae* collected from different depths within a stratified lake. *Eur J Phycol.* 1999;34:477–485.
43. Krivtsov V, Bellinger EG, Sigeo DC. Modelling of elemental associations in *Anabaena*. *Hydrobiologia* 1999;414:77–83.
44. Krivtsov V, Bellinger EG, Sigeo DC. Elemental composition of *Microcystis aeruginosa* under conditions of lake nutrient depletion. *Aquatic Ecol.* 2005;39:123–134.
45. Ho T-Y, Quigg A, Zoe V, Milligan AJ, Falkowski PG, Morel FMM. The elemental composition of some marine phytoplankton. *J Phycol.* 2003;39:1145–1159.
46. Liehr SK, Wayland Eheart J, Suidan MT. A modeling study of the effect of pH on carbon limited algal biofilms. *Water Res.* 1988;22:1033–1041.
47. Brindley C, Acien FG, Fernandez-Sevilla JM. The oxygen evolution methodology affects photosynthetic rate measurements of microalgae in well-defined light regimes. *Biotechnol Bioeng.* 2010;106:228–237.
48. Marquez FJ, Sasaki K, Nishio N, Nagai S. Inhibitory effect of oxygen accumulation on the growth of *Spirulina platensis*. *Biotechnol Lett.* 1995;17:225–228.
49. Asenjo J, Merchuk J. *Bioreactor System Design*. New York: Marcel Dekker; 1995.
50. Falkner R, Falkner G. Distinct adaptivity during phosphate uptake by the cyanobacterium *Anabaena variabilis* reflects information processing about preceding phosphate supply. *J Trace Microprobe Tech.* 2003;21:363–375.
51. Riegman R, Mur LR. Regulation of phosphate uptake kinetics in *Oscillatoria agardhii* Arch Microbiol. 1984;139:28–32.
52. Kromkamp J. Formation and functional significance of storage products in cyanobacteria. *New Zeal J Mar Freshwater Res.* 1987;21:457–465.
53. Anderson LA. On the hydrogen and oxygen content of marine phytoplankton. *Deep-Sea Res Part I.* 1995;42:1675–1680.
54. Berberoglu H, Barra H, Pilon L, Jay J. Growth, CO<sub>2</sub> consumption, and H<sub>2</sub> production of *Anabaena variabilis* ATCC 29413-U under different irradiances and CO<sub>2</sub> concentrations. *J Appl Microbiol.* 2008;104:105–121.
55. Macedo MF, Ferreira JG, Duarte P. Dynamic behaviour of photosynthesis-irradiance curves determined from oxygen production during variable incubation periods. *Mar Ecol Prog Ser.* 1998;165:31–43.
56. Markou G, Chatzipavlidis I, Georgakakis D. Effects of phosphorus concentration and light intensity on the biomass composition of *Arthrospira (Spirulina) platensis*. *World J Microbiol Biotechnol.* 2012;28:2661–2670.
57. Stewart PS. Diffusion in biofilms. *J Bacteriol.* 2003;185:1485–1491.
58. Kreft JU, Picioreanu C, Wimpenny JW, Loosdrecht MC. Individual-based modelling of biofilms. *Microbiology* 2001;147:2897–912.
59. Fan LS, Leyvaramos R, Wisecarver KD, Zehner BJ. Diffusion of phenol through a biofilm grown on activated carbon particles in a draft-tube 3-phase fluidized-bed reactor. *Biotechnol Bioeng.* 1990;35:279–286.
60. Mu D, Liu Z-S, Huang C, Djilali N. Determination of the effective diffusion coefficient in porous media including Knudsen effects. *Microfluid Nanofluid* 2007;4:257–260.
61. Incropera FP, Dewitt DP, Bergman TL, Lavine AS. *Fundamentals of Heat and Mass Transfer*, 6th ed. Hoboken, NJ: John Wiley & Sons; 2007.
62. Gustafsson JP. *Visual MINTEQ*. Stockholm: KTH, Department of Sustainable Development, Environmental Science and Engineering; 2011. <http://www2.lwr.kth.se/English/OurSoftware/vminteq/>. Accessed Nov 20, 2013.
63. Norsker N-H, Barbosa MJ, Vermuë MH, Wijffels RH. Microalgal production—a close look at the economics *Biotechnol Adv.* 2011;29:24–27.
64. Murphy TE. Artificial leaf for biofuel production and harvesting: Transport phenomena and energy conversion (Ph.D. dissertation). The University of Texas at Austin. 2013.
65. Mandalam RK, Palsson BO. Elemental balancing of biomass and medium composition enhances growth capacity in high-density *Chlorella vulgaris* cultures. *Biotechnol Bioeng.* 1998;59:605–611.
66. Danquah MK, Harun R, Halim R, Forde GM. Cultivation medium design via elemental balancing for *Tetraselmis suecica*. *Chem Biochem Eng Q.* 2010;24:361–369.